Composites Science and Technology 216 (2021) 109041

Contents lists available at ScienceDirect

Composites Science and Technology

journal homepage: www.elsevier.com/locate/compscitech

Coaxial 3D-Printed and kirigami-inspired deployable wearable electronics for complex body surfaces

Shuaishuai Zhang [a], Sheng Wang [a], Yuxiang Zheng [b], Run Yang [b], Erbao Dong [b], Liang Lu [c], Shouhu Xuan [a,**], Xinglong Gong [a,*]

[a] CAS Key Laboratory of Mechanical Behavior and Design of Materials, Department of Modern Mechanics, University of Science and Technology of China (USTC), Hefei, Anhui, 230027, PR China

[b] Department of Precision Machinery and Precision Instrumentation, University of Science and Technology of China (USTC), Hefei, Anhui, 230027, PR China

[c] The First Affiliated Hospital of USTC, Division of Life Sciences and Medicine, University of Science and Technology of China, Hefei, Anhui, 230036, PR China

ARTICLE INFO

Keywords:
Shear stiffening
Core-sheath fiber
Kirigami
Deployable devices
Human-robot interaction

ABSTRACT

Wearable electronics used to capture biological signals are substantially important in human–robot interactions, health monitoring, and clinical treatment. However, for curved or irregular body surfaces, intimate interfacing with the skin, which is essential for robust signal recording, is challenging. In this study, flexible core-sheath fiber sensors and adaptive devices were developed using a coaxial 3D printing technique and kirigami-inspired patterns. The printed core-sheath fiber, which was successfully applied in human–robot interaction, exhibited excellent electromechanical properties with a sensing strain range of 700%, and had high accuracy of approximately 3 mN and high electromechanical durability. In addition, the viscoelastic nature of the core material (shear-stiffening gel) provided the fiber array with fine energy dissipation performance against external harm by buffering the impact force by 51% while simultaneously capturing the dynamic impact in 4 ms. Moreover, the introduction of kirigami-inspired deformability to planar electronics facilitated conformable attachment of sensing devices with substantial adjustability to 3D curved surfaces; they can be adapted to shoe pads of different sizes without compromising their sensitivity. The 3D printing technique and kirigami-inspired pattern designs for creating adaptive and flexible wearable electronics hold great potential for advanced health monitoring of diverse and complex epidermal surfaces.

1. Introduction

Wearable electronics have gained increasing interest owing to their potential applications in health monitoring systems [1,2], medical prostheses, and intelligent robotics [3,4]. Traditional fabrication methods for preparing wearable electronics, such as photolithography [5], laser writing [6], and metal deposition [7] have limitations, such as complicated processes, high cost, and uncontrollability. The emerging 3D printing technique, which has scalability and controllability, has provided a new strategy for developing wearable electronics in a programmable manner [8–10]. 3D-Printed sensors, which have high sensitivity and low detection limit, are capable of differentiating human movements [11,12] and monitoring biological signals [8,13,14]. However, these sensors are normally directly exposed to the natural environment without any protection, which may result in a shortened service life and rapid performance degradation. To withstand unfavorable environments, several methods, such as spray coating [15], injection into microchannels [16], and droplet deposition have been used to protect sensors with protective layers [17]. In addition, the coaxial 3D printing technique provides a highly efficient, simple, and scalable approach for fabricating complex core-sheath structures that overcome the limitations of the abovementioned methods. For example, a liquid metal can be directly encapsulated into an elastomeric sheath in a single step through coaxial extrusion without any post-processing, such as injecting or casting [18]. A flexible core-sheath sensor, which can monitor and differentiate human joint motions, was fabricated through the coaxial extrusion of conductive and elastomeric inks [19]. Thus, the coaxial 3D printing technique is a useful and feasible way to develop high-performance and steady core-sheath sensors for wearable electronics.

* Corresponding author.
** Corresponding author.
E-mail addresses: xuansh@ustc.edu.cn (S. Xuan), gongxl@ustc.edu.cn (X. Gong).

https://doi.org/10.1016/j.compscitech.2021.109041
Received 22 February 2021; Received in revised form 9 July 2021; Accepted 11 September 2021
Available online 16 September 2021

Most skin-mounted wearable electronics for human motion detection and health monitoring have been presented in a soft planar form [20–22]. A more complicated structure is required to achieve an intimate interface with the skin for physiological sensing. Recently, the ancient art of paper cutting (kirigami), which transforms planar 2D structures into complex 3D structures, has gained increasing attention [23–25]. Much effort has been devoted to introducing kirigami patterns to wearable electronics to develop advanced functions and widen their applications [26,27]. The strain accommodations of the sensors can be extended 20 fold without compromising the electrical conductivity or fluorescence property through geometric engineering of the polymer sheets into kirigami patterns [28]. Moreover, a kirigami scheme for constructing 3D deformable electronic systems has been successfully developed to make wearable devices conformably attached to 3D curved surfaces with minimal invasiveness while maintaining stable mechanical and electrical properties [29]. These devices can be self-adaptive for more robust adhesion to body surfaces, which benefits the monitoring of external stimuli. However, external stimuli in our daily lives, such as violent collisions and shocks, may be harmful to individuals, and cause serious body injuries. Thus, more effort should be devoted to ensuring personal safety.

However, the increasing awareness of security has propelled the development of wearable electronics with the ability to warn and protect people from danger [30]. An ultrasensitive and highly fire-retardant aerogel device is developed for fire warning [31]. Based on the combined mechanical and thermal effects of porous graphene, wearable devices with integrated alarm functions have been successfully applied to warn people of potential abnormal health conditions [32]. However, the protective performance of these electronics is still limited, which restricts their practical applications. Shear-stiffening gel (SSG)-based composites, with excellent electromechanical properties and safeguarding performance, have gained increasing attention owing to their prospective anti-impact and sensing capabilities [33,34]. Due to the impregnation of SSG, the impact resistance of Kevlar fabrics was improved by 150%, thus finding applicability in soft body armor [35]. Conductive SSG-based sensors exhibit outstanding electromechanical properties with gauge factors greater than 500 that can even capture the footsteps of a small spider, indicating a promising potential for wearable electronics [36]. Therefore, SSG-based smart wearable electronics may be a suitable choice for monitoring biological signals and protecting people from external harm.

In this work, we developed an SSG-based core-sheath fiber sensor for wearable electronics and kirigami-inspired deployable devices to make them conformably attached to curved and size-varied surfaces. The core-sheath fiber sensor, fabricated using the coaxial 3D printing technique, can capture stretch, compression, and bending deformations with an outstanding accuracy of approximately 3 mN, excellent electrical durability (>10000 cycles), and superior mechanical stability. Furthermore, it has been well applied in human–robot interaction, accomplishing missions, including human gesture capturing, robot arm control, and feedback. Owing to the rate-dependent electromechanical properties, the core-sheath fiber-based arrays could not only detect external static and dynamic stimuli, but also buffer the impact force by 51%, exhibiting superior safeguarding performance. Moreover, the kirigami-inspired patterns transformed the 2D planar wearable electronics into 3D adjustable structures, which could adjust themselves to curved or size-varied surfaces. This method for fabricating adjustable sensing devices has promising potential for functional wearable electronics.

2. Experiment section

2.1. Materials

Ethanol and boric acid were purchased from Sinopharm Chemical Reagent Co., Ltd. (Shanghai, China). Hydroxyl silicone oil (Polydimethylsiloxane, PDMS, 500 mm^2/s, AR degree, Jining Huakai Resin Co., Ltd.) was used to prepare an SSG. Conductive multiwall carbon nanotubes (CNT, type: TF-25001) were obtained from Tan Feng Co., Ltd. Commercially available silicone elastomer (Ecoflex 00200), Thi-Vex silicone thickener, and Slo-Jo platinum silicone cure retarder were purchased from Smooth-On (Macungie, PA, USA). Silicone oil (Sinopharm Chemical Reagent Co., Ltd.) was used for an oil bath. A polyethylene terephthalate (PET) film (thickness: 0.1 mm) was used as a flexible substrate for the 3D printing of the fiber film.

2.2. Preparation of printing inks

First, 1 g of boric acid, 40 mL of hydroxyl silicone oil, and a certain volume fraction of CNT were mixed evenly in a ceramic dish by continuously stirring for 10 min. The mixture was then heated at 180 °C for 1.5 h and stirred every 15 min to ensure a homogeneous reaction. The mixture formed a lightly cross-linked, sticky, and viscous gel during heating. After cooling to room temperature, core inks (SSG or SSG-CNT) were obtained. This polymer was named as SSG-xCNT and x represented the volume fraction.

Ten grams each of Ecoflex 00–20 Part A and Part B were mixed homogeneously. Then, 0.5 g of Thi-Vex silicone thickener (referred to as Thi) was added as a rheological modifier, and 0.2 g of Slo-Jo platinum silicone cure retarder was used to increase the pot life. The mixture was then transferred to a 20 mL syringe and degassed in a planetary centrifuge (HM800, Shenzhen Hasai Technology Co., Ltd., Shenzhen, China) at 3000 rpm for 15 min to obtain the sheath ink.

2.3. Printing of core-sheath fiber and patterns

The coaxial nozzles were constructed using an Object260 Connex3 PloyJet 3D multimaterial printer (Statasys Ltd.). A 20 mL pneumatic syringe was used to store the core inks (SSG-CNT). An air cylinder connected to an air compressor and a pressure regulator (XN2010, Puma Industrial Co., Ltd.) were used to provide an appropriate pressure of 0.6 MPa to extrude the core inks through the inner nozzle. A syringe pump (LSP02-1B, Longer Pump Co., Ltd.) was used to extrude the sheath ink (liquid Ecoflex) through the outer nozzle at a speed of 0.8 mm^3/s. The core-sheath fiber was coextruded into an oil bath pot and heated at 60 °C for 15 min. Then, the fiber was transferred to an oven at 80 °C to vulcanize the Ecoflex sheath for 15 min. Then, coaxial nozzles were assembled on a computer-controlled 2-axis movement platform (VG-L5S, Vigotec Co., Ltd.). The core-sheath fiber patterns were printed following the paths designed by the VigoEngravel software. Then, the printed patterns were vulcanized in an oven at 80 °C for 15 min to obtain the final products.

2.4. Characterization

The morphologies of the CNT, SSG, and SSG-CNT/Ecoflex composite fibers were characterized using field emission scanning electron microscopy (FE-SEM, XL30 ESEM). The rheological properties of the inks were characterized using a stress-controlled rheometer (Physica MCR302, Anton Paar Co., Austria). The stretch and compression tests were carried out using a dynamic mechanical analyzer (DMA, Electro Force 3200, TA instruments, Minnesota, USA). The Modulab® material test system (Solartron Analytical, AMETEK Advanced Measurement Technology, Inc., United Kingdom) was used to evaluate the electrical performance of the core-sheath fiber, and the sampling frequency was set at 1000 Hz. The impact tests were carried out on a drop tower machine (ZCJ1302-A, MTS System Co., America) with a drop hammer mass of 0.25 kg.

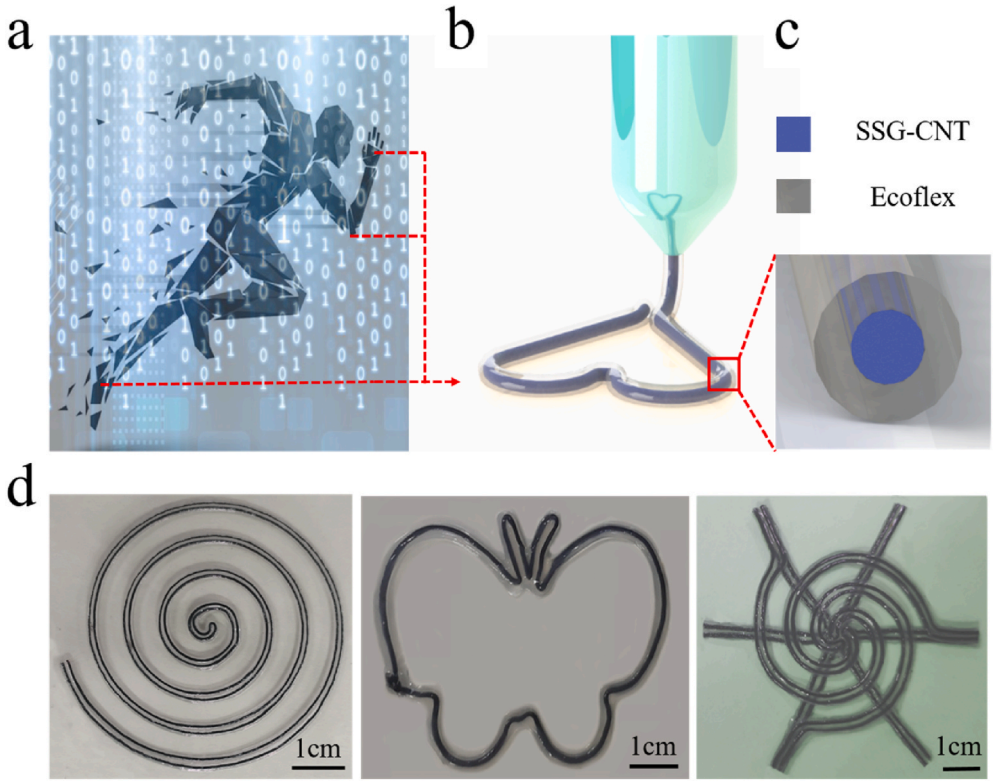

Fig. 1. Fabrication process of the core-sheath fibers and SSG-CNT/Ecoflex composites patterns. Detection of human body movements (a). Illustration of the coaxial 3D printing process of SSG-CNT/Ecoflex patterns (b). Section view of the core-sheath structure (c). 3D Printing of core-sheath fiber into several patterns: logarithmic-spiral, butterfly, and spider web (d).

3. Results and discussion

3.1. 3D printing of core-sheath fibers and SSG-CNT/Ecoflex composite patterns

Fig. 1a shows a schematic of the 3D printed core-sheath fiber sensors for human motion monitoring, such as hand gesture, elbow bending, and gait. Using the 3D coaxial printing technique, the core and sheath inks were coextruded from the coaxial nozzle (Fig. 1b and S1), forming a steady core-sheath structured fiber (Fig. 1c). Fiber sensors can be obtained by assembling copper electrodes without other complex post-processes. In addition, the core-sheath fiber can also be smoothly 3D-printed into various patterns, such as logarithmic-spiral, butterfly, and spider web patterns, exhibiting the advantages of customization and scalability (Fig. 1d).

Suitable printing inks were prepared by investigating their rheological properties. The pristine SSG exhibited a typical shear-stiffening behavior, and its storage modulus (G') increased dramatically with shear frequency (Fig. 2a). At 0.1 Hz, G' was 166 Pa, and the SSG was soft and plastic. As the shear frequency increased to 100 Hz, G' increased by 3 orders of magnitude to approximately 0.2 MPa, which exhibited a solid characteristic. During the fabrication of the SSG, the hydroxyl silicone oil was successfully cross-linked via chemical "Si–O–B" bonds with the introduction of boric acid. More importantly, the physical crosslinks between boron and oxygen atoms from different molecules were incorporated [37]. In contrast to permanently connected chemical bonds, physical crosslinks can undergo rate-dependent breaking and reattaching processes, which results in a unique shear-stiffening behavior. At a low strain rate, these dynamic crosslinks could break and reattach freely and carry almost no load. Therefore, the SSG will be in a viscous liquid state and can be deformed easily. At a high strain rate, there is not enough time for the attached physical crosslinks to break. The attached physical crosslinks behave like permanent chemical bonds and severely restrict the deformation. Thus, the SSG is transformed into a rubbery state, exhibiting a much larger modulus [38].

The CNT strengthened the mechanical performance of the SSG. As the CNT volume fraction (φ) was 3.79%, the G' at 0.1 Hz and 100 Hz increased to 628 Pa and 0.28 MPa, respectively. G' increased with φ, which could be explained using the cluster-cluster-aggregation model [39]:

$$G' - G'_{SSG} \propto \varphi^{(3+B)/(3-N)} \quad (1)$$

where B and N are the fractal dimensions of the network and its backbone, respectively (Fig. 2b). As expected, the data followed a power law with an exponent of 2.1. In the shear strain sweep tests, G was steady at low strain and tended to decrease with increasing strain for all composites due to Payne effect [40] (Fig. 2c). The red points indicated the strain at which the composites began to yield. The yield strain (γ_c) reduced with φ following a power law with an exponent of −1.09 (Fig. S2). Consistent with its highly liquid-like nature, the dynamic viscosity ($\eta' = G''/\omega$) of the SSG was relatively low at approximately 7000 Pa s (Fig. S3), which facilitated the smooth extrusion of the SSG-CNT through the inner nozzle.

Creep is the tendency of a solid material to deform slowly under the loading of external stress. It has been widely studied to demonstrate the viscoelastic properties of polymer composites. In this work, the creep (red part) and recovery behaviors (green part) of the SSG and SSG-CNT composites were investigated (Fig. 2d). When a shear stress of 5 Pa was applied for 300 s, the shear strain (γ) of the SSG increased linearly to approximately 16.2% owing to its lightly cross-linked nature. As the shear stress was removed, γ remained almost unchanged for following 600 s with an unrecoverable strain of 16.0%. The introduction of CNT enhanced the strength of the SSG-CNT composites. At the creep stage, the introduction of 3.79% CNTs reduced γ to 6.8%. At 300 s, γ decreased with increasing φ. Moreover, SSG-CNT recovered more quickly than SSG

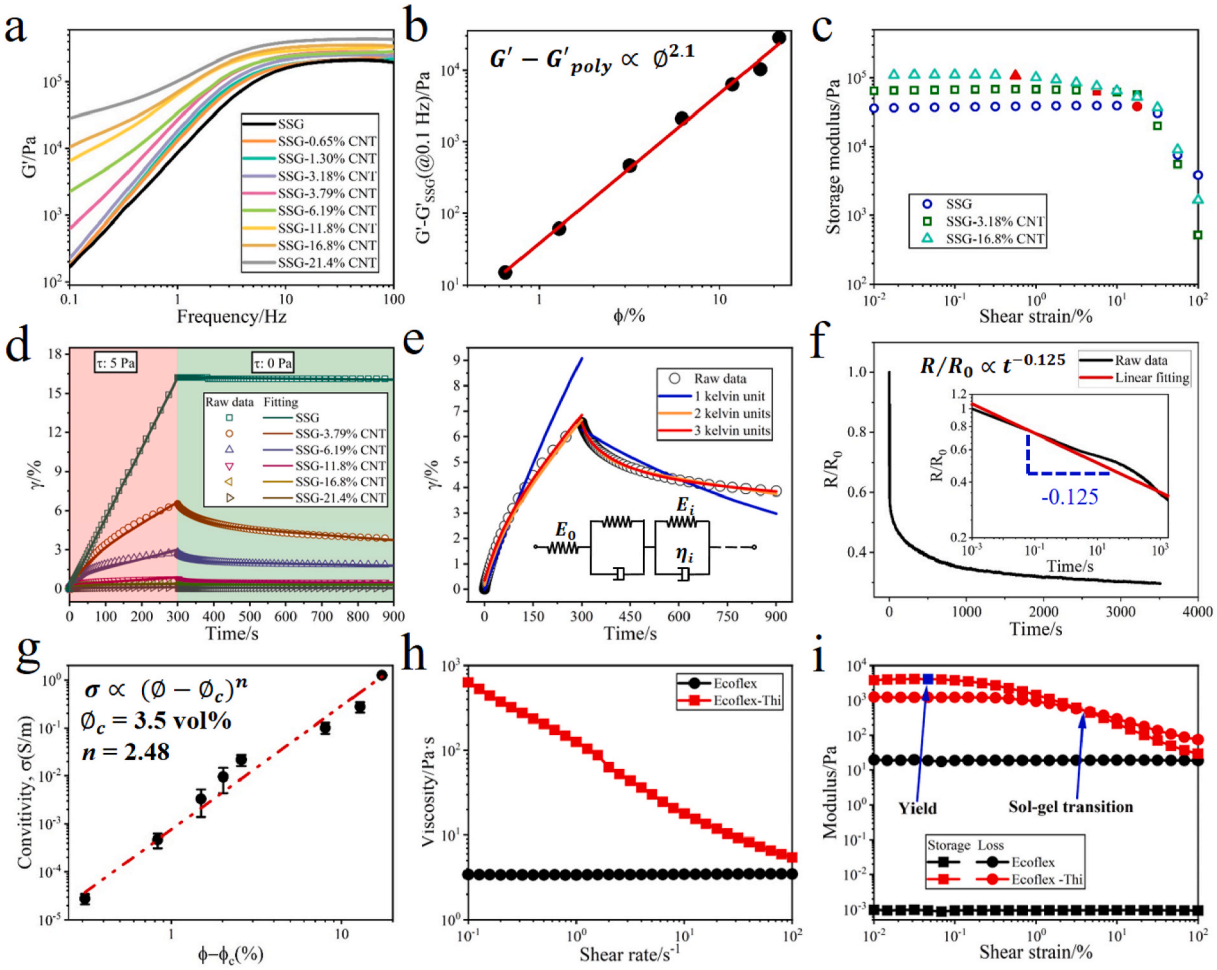

Fig. 2. Rheological and electrical properties of the printing inks. Storage modulus of the SSG and SSG-CNT at various shear frequencies (a). Storage modulus at 0.1 Hz plotted against CNT volume fraction (φ); the solid red line is a fit to Eq. (1) (b). Storage modulus against shear strain at a shear frequency of 1 Hz (c). Results of shear creep tests (d). Comparison between raw data and fittings with different Kelvin units at $\varphi = 3.79\%$ (e). Time evolution of the electrical resistance of the SSG-CNT ($\varphi = 3.79\%$); the inset image is the log-log plot and linear fitting (f). Electrical conductivity (σ) as a function of reduced CNT volume fraction ($\varphi - \varphi_c$), where φ_c is the electrical percolation threshold (g). Viscosity (h) and modulus (i) of uncured liquid Ecoflex with/without rheological modifier (Thi). (For interpretation of the references to colour in this figure legend, the reader is referred to the Web version of this article.)

as the shear stress was removed, indicating a stronger resilience. The creep behavior of the SSG-CNT (φ: 3.79%) could be explained by the generalized Kelvin model, where a spring (E_0) is connected in series with n Kelvin units (Fig. 2e). The shear strain γ is expressed as follows:

$$\gamma = \begin{cases} \sigma_0\left(\frac{1}{E_0} + \sum\frac{1}{E_i}\left(1 - e^{-t/\tau_i}\right)\right) & t < t_0, \\ \sigma_0\left(\sum\frac{1}{E_i}\left(e^{-(t-t_0)/\tau_i} - e^{-t/\tau_i}\right)\right) & t > t_0, \end{cases} \quad (2)$$

where $\tau_i = \eta_i/E_i$ is the characteristic relaxation time of the ith Kelvin unit, and $t_0 = 300$ s. Apparently, the model with only 1 K unit did not agree with the creep data. Increasing the Kelvin units to two improved the fitting results remarkably, with a correlation of 0.99. A further increase in Kelvin units had a very limited impact on the final results. Thus, a generalized Kelvin model with 2 K units was adopted here, and the fitting results explained the creep data well, as shown in Fig. 2d.

In contrast to the normal time-irrelevant conductivity of most sensors, the resistance of the SSG-CNT decayed rapidly initially and then gradually became steady (Fig. 2f). The resistance decay followed a power law (Fig. 2f, inset).

$$\frac{R}{R_0} \propto t^{-0.125} \quad (3)$$

where R is the resistance at time t, and R_0 is the resistance at $t = 0$. Owing to the high viscoelasticity and low modulus of the SSG, the conductive fillers (CNT) were relatively mobile and could move by diffusion. This allowed the conductive network to relax slowly, thereby forming more connections and causing resistance decay [36,41]. The electrical conductivity of the SSG-CNT increased rapidly with CNT volume, reaching approximately 0.1 S/m at 11.8 vol% (Fig. 2g). Based on the percolation theory [42,43], the conductivity scaled with a filler volume fraction φ is

$$\sigma \propto (\varphi - \varphi_c)^n \quad (4)$$

where φ_c and n are the percolation threshold and exponent, respectively. The equation fitted the data well, giving $\varphi_c = 3.5\%$ and $n = 2.48$. According to previous research, and based on Fig. S4, piezoresistance sensors with a volume fraction slightly larger than φ_c are preferred owing to their higher sensitivity [44]. Thus, SSG-3.79%CNT was used in the following study, which was defined as SSG-CNT for simplicity.

A suitable sheath ink was prepared by studying the rheological properties of uncured liquid Ecoflex. Liquid Ecoflex with a rheological modifier (Thi) exhibited a remarkable shear-thinning behavior, allowing it to flow smoothly through the nozzle during the printing process (Fig. 2h). The storage modulus of liquid Ecoflex was relatively lower than its loss modulus, indicating a liquid-like characteristic (Fig. 2i). Owing to the rheological modifier, the storage modulus of liquid

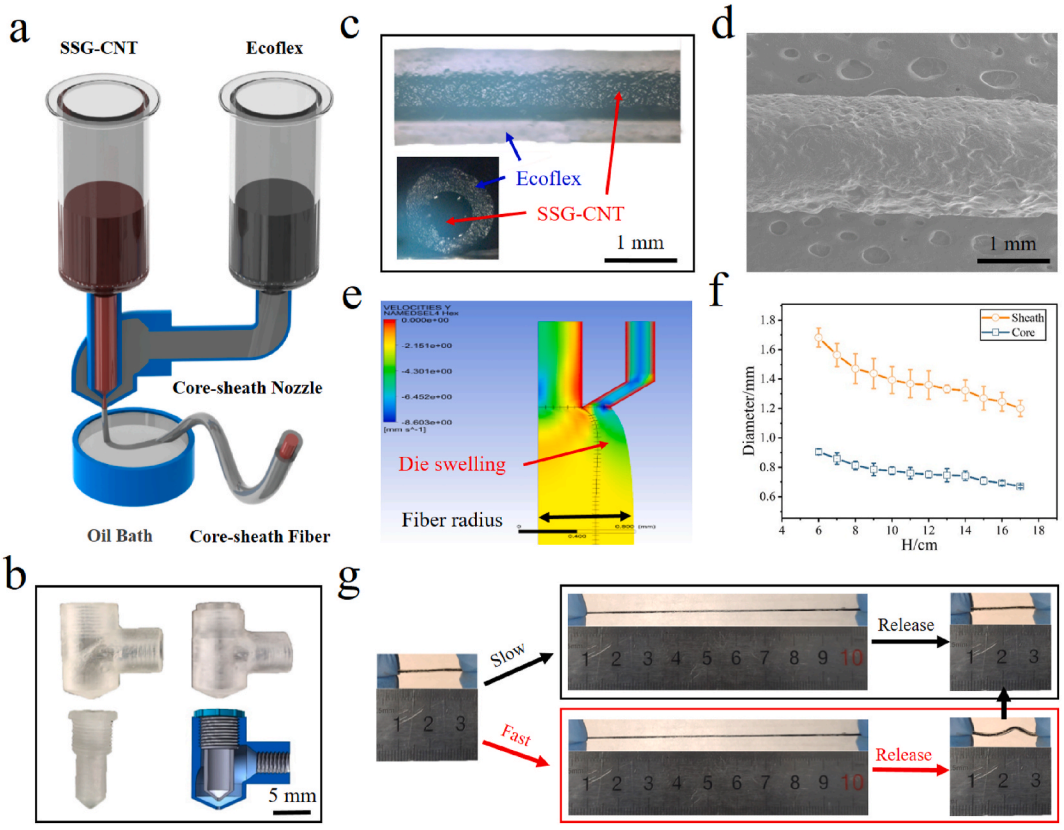

Fig. 3. Fabrication of the core-sheath fiber. Schematic of the fabrication of the core-sheath fiber (a). Photos of the inner nozzle (bottom left), outer nozzle (upper left), coaxial nozzle (upper right), and schematic section view (bottom right) of the coaxial nozzle (b). Microscopic and SEM images of the side and cross-sectional view of the core-sheath fiber (c and d). Simulation result of the die swelling phenomenon during the co-extrusion process (e). Core and sheath diameters vs. height (*H*) from the nozzle to the oil surface (f). Images of the core-sheath fiber in the original, stretched, and recovered states during the slow and fast stretch conditions (g).

Ecoflex-Thi reached 1244 Pa, which was relatively higher than the corresponding loss modulus at 0.01% strain. This result indicates that Ecoflex-Thi exhibits a solid-like characteristic in the static state, which is essential for printing self-supported structures. The sol–gel transition strain and stress were approximately 3.16% and 26 Pa, respectively. The low sol–gel transition strain/stress guaranteed the fluent extrusion of liquid Ecoflex through the nozzle.

Owing to their outstanding printability, the SSG-CNT and liquid

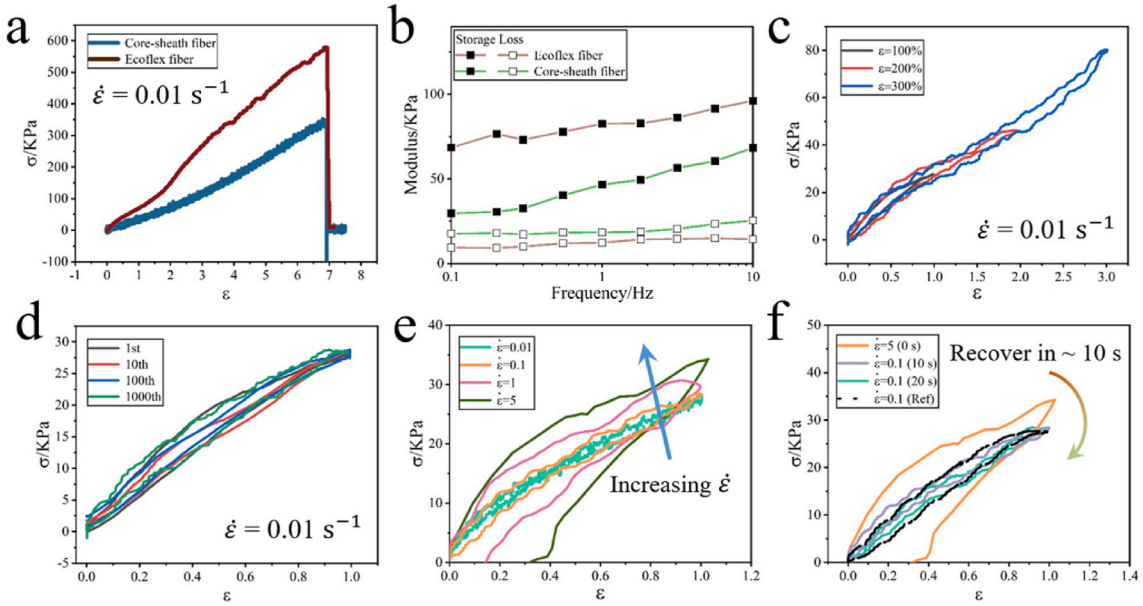

Fig. 4. Mechanical property of core-sheath fiber. Stress (σ) vs. strain (ε) of Ecoflex fiber and core-sheath fiber at strain rate $\dot{\varepsilon} = 0.01\ s^{-1}$ (a). Storage/loss modulus of Ecoflex fiber and core-sheath fiber plotted against tensile frequency (b). Stresses (σ) of the core-sheath fiber under 1, 2, and 3 tensile strain at $\dot{\varepsilon} = 0.01\ s^{-1}$ (c). Cyclic tensile tests at $\dot{\varepsilon} = 0.01\ s^{-1}$ (d). Tensile tests with increasing $\dot{\varepsilon}$ (e). Mechanical recovery presentation of core-sheath fiber after tensile tests at high strain rate (f).

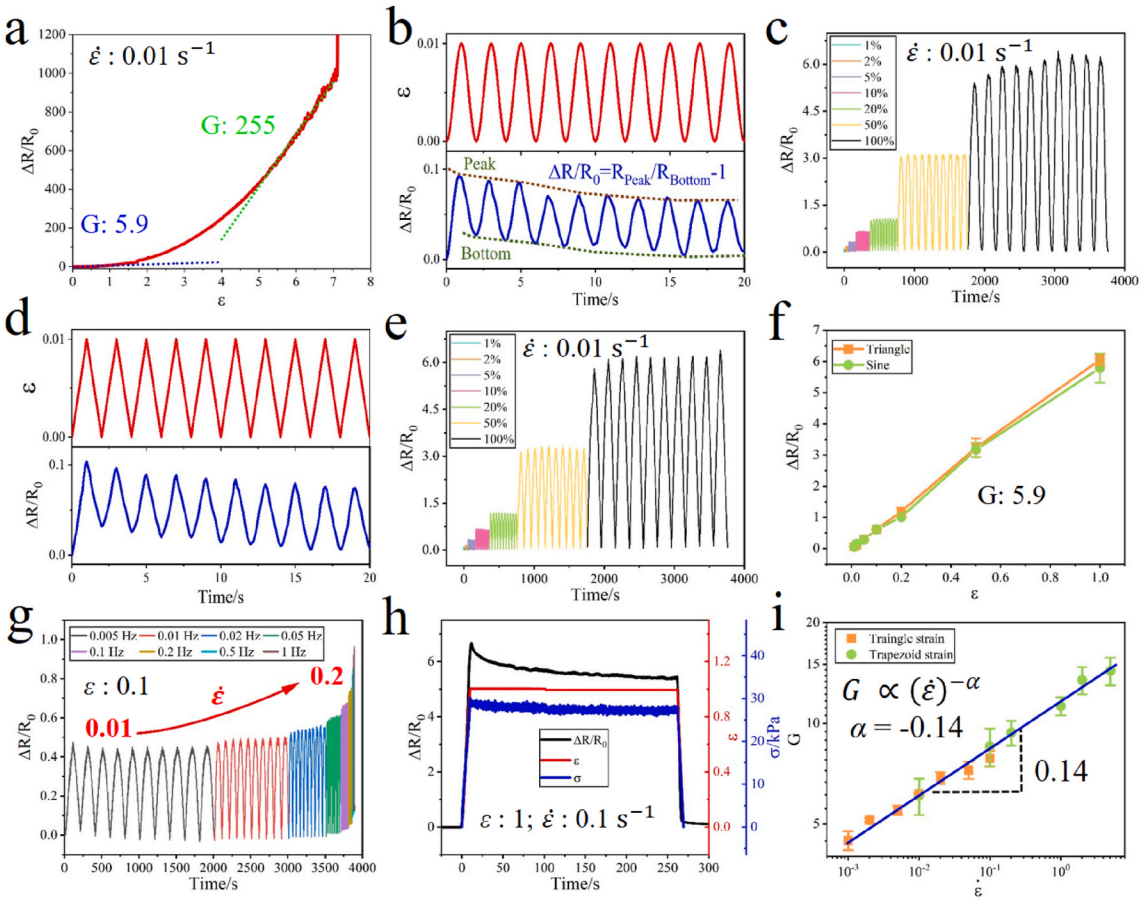

Fig. 5. Electromechanical property of the core-sheath fiber under tensile loadings. Relative resistance change ($\Delta R/R_0$) of the core-sheath fiber under tensile strain loadings (a). $\Delta R/R_0$ as a function of time under repeated 0.01 sinusoidal strain (b) and varying sinusoidal strain loadings (c). $\Delta R/R_0$ at repeated 0.01 triangular strain (d) and varying triangular strain loadings (e). $\Delta R/R_0$ plotted vs strain (f). $\Delta R/R_0$ at repeated 0.1 strain and increasing strain rate, $\dot{\varepsilon}$ (g). $\Delta R/R_0$, strain and stress vs. time in trapezoidal strain waveform (h). Sensitivity gauge (G) plotted vs. strain rate, $\dot{\varepsilon}$ (i).

Ecoflex were coextruded smoothly by the air and syringe pumps through the coaxial nozzle (Fig. 3a and S4), which was composed of two cylindrical nozzles aligned coaxially. The inner nozzle (Fig. 3b, bottom left) was tightly assembled within the outer nozzle (upper left), forming a coaxial nozzle (upper right). Based on the schematic cross-sectional view of the coaxial nozzle (bottom right), the coaxial channels for the printing inks were constructed. The outlet diameters of the inner and outer nozzles were 0.6 and 1.0 mm, respectively. The outer nozzle was prefilled with sheath ink to seal the front drop of the extruded inner ink. After extrusion, a steady core-sheath structure was built and dropped into the oil bath pot from a certain height (H). After vulcanization, a core-sheath fiber was obtained.

The SSG-CNT core was located in the center of the fiber and thoroughly and tightly wrapped by the Ecoflex sheath, which resisted the cold-flow nature of SSG-CNT (Fig. 3c). The fiber exhibited a uniform diameter (~1.32 mm), which proved the effectiveness and practicality of the printing process (Fig. 3d and S6). Using this fabrication process, a large coil of core-sheath fiber could be fabricated, exhibiting a capability for mass production, which was relevant for industrial application (Fig. S7). Interestingly, the fiber diameter was larger than the nozzle outlet diameter (1 mm) due to the die swelling phenomenon [45]. The highly viscoelastic SSG was subjected to a strong extrusion in the nozzle, causing elastic deformation. After the SSG left the nozzle die, the external constraints disappeared. Thus, elastic recovery occurred in the SSG, resulting in swelling (Fig. 3e). Owing to gravity, the core and sheath diameters of the fiber decreased as H (the height from the nozzle to the oil surface) increased (Fig. 3f). For example, as H increased from 6 to 14 cm, the core and sheath diameter decreased from 0.90 to 1.68 mm to 0.74 and 1.32 mm, respectively. Owing to the superior flexibility of the Ecoflex sheath, the core-sheath fiber could be stretched by 400% (Fig. 3g). Moreover, the fiber exhibited a rate-dependent property owing to the viscoelasticity of the SSG. After the fiber was stretched and released slowly, it immediately returned to its initial length. When the fiber was stretched quickly, a residual strain occurred after the release. However, the fiber could recover completely in approximately 10 s owing to the elastic property of the Ecoflex sheath, which suppressed the liquid-flow nature of the SSG.

3.2. Electromechanical property of core-sheath fiber

To comprehensively illustrate the mechanical properties of the core-sheath fibers, tensile tests were carried out at different strains (ε) and strain rates ($\dot{\varepsilon}$). First, the core-sheath and Ecoflex fibers were stretched until break at $\dot{\varepsilon} = 0.01\ s^{-1}$ (Fig. 4a). Apparently, the pristine Ecoflex fiber exhibited a higher Young's modulus ($E = \sigma/\varepsilon$, ~70 kPa) than the core-sheath fiber (~27 kPa). In addition, the high extensibility of Ecoflex allowed both fibers to remain intact until approximately 700% strain, exhibiting superior stretchability. Dynamic tensile tests were then performed to characterize the dynamic properties of the fibers (Fig. 4b). The fibers with a test length of 20 mm were stretched by 20% strain, and then, a sine wave with a magnitude of 5% strain was applied. The frequency increased exponentially from 0.1 to 10 Hz. The loss modulus of both fibers were lower than their storage modulus owing to the elasticity of Ecoflex. Due to the introduction of viscoelastic SSG, the loss modulus of the core-sheath fiber became relatively larger, indicating a better energy damping capability.

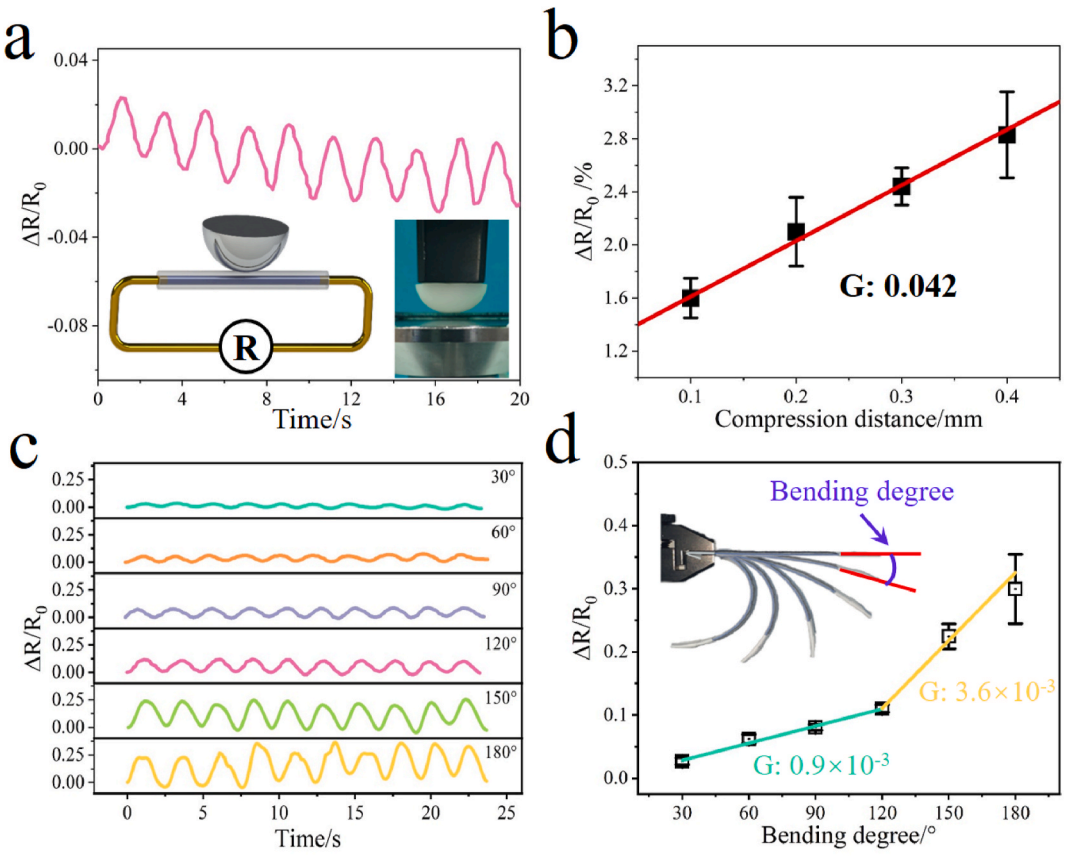

Fig. 6. Electromechanical property of the core-sheath fiber at compression and bending loadings. $\Delta R/R_0$ of the core-sheath fiber under 0.2 mm compression tests and the setup of compression tests (inset) (a). Plot of $\Delta R/R_0$ vs. compression distance (b). $\Delta R/R_0$ as a function of time under increasing bending loadings (c). Plot of $\Delta R/R_0$ vs. bending loading (d).

The mechanical stability of the core-sheath fiber was characterized through cyclic tensile tests. When the tensile strains were 1, 2, and 3, the stress values reached 26.8, 45.9, and 80.2 kPa, respectively (Fig. 4c). After the 1000th stretch cycle, the stress–strain curves shifted slightly, indicating the remarkable mechanical stability of the core-sheath fiber (Fig. 4d). Owing to the SSG-CNT core, the core-sheath fiber also exhibited a typical rate-dependent property (Fig. 4e). For example, as the $\dot{\varepsilon}$ increased from 0.01 to 5 s^{-1}, the maximum stress increased from 27.0 to 34.2 kPa. Moreover, the release stress was relatively lower and quickly declined to zero before the fiber was fully released at $\dot{\varepsilon} = 5\ s^{-1}$. The mechanical recovery performance of the fiber is shown in Fig. 4f. During the stretching and releasing process, the stress–strain curves at $\dot{\varepsilon} = 0.1\ s^{-1}$ showed a small difference (Ref). After the release, the stress in the fiber returned to zero, indicating that the fiber recovered to its initial state. After stretching and releasing at $\dot{\varepsilon} = 5\ s^{-1}$, the core-sheath fiber was in a relaxed state. After 10 s, the fiber was stretched again at $\dot{\varepsilon} = 0.1s^{-1}$. The fiber exhibited strain–stress behaviors similar to those of the pristine fiber after recovery for 10 s, and the final stress returned to zero after the release. Owing to the elasticity of the Ecoflex sheath, the fiber exhibited a quick and complete mechanical recovery behavior in a short time. Thus, the core-sheath fiber, with typical viscoelasticity, flexibility, and mechanical stability, is a promising candidate for multifunctional wearable electronics.

Due to the introduction of conductive CNT, the core-sheath fiber exhibited superior electromechanical properties and showed high potential for use in flexible sensors. Thus, tensile tests were carried out on the core-sheath fibers. The relative resistance change ($\Delta R/R_0$) increased with the applied tensile strain (Fig. 5a). Here, ΔR is the increment in resistance from time $t = 0$ (R_0) to time t (R). The gauge factor (G), which represents the sensitivity of the sensor, was calculated as $G = \frac{\Delta R}{R_0}/\varepsilon$. The $\Delta R/R_0$ value presented two linear correlation regions. The calculated G values of the sensor were 5.9 and 255 for strains ranging from 0 to 1 and 5 to 7, respectively. In the cyclic tensile tests, the resistance of the core-sheath fiber sensor increased as it was stretched. When it was released, the resistance was gradually recovered (Fig. 5b). Moreover, it exhibited a repeated resistance response to small cyclic strain (0.01) and low stress (~270 Pa), indicating superior stability and excellent accuracy. Additionally, in each cycle, the resistance at zero strain was smaller than the former due to resistance decay effect; thus, $\Delta R/R_0$ was modified as follows:

$$\frac{\Delta R}{R_0} = \frac{R_{Peak}}{R_{Bottom}} - 1 \tag{5}$$

where R_{Peak} and R_{Bottom} are the resistance values at the largest and zero strains at the same tensile cycle, respectively. At a constant strain rate of 0.01, the electrical response increased with the applied strain, which varied from 0.01 to 1 (Fig. 5c and e). Furthermore, as the applied strain was set to have a certain relationship with time, such as that forming a sinusoidal waveform (Fig. 5b) or triangular waveform (Fig. 5d), the electrical signal response was consistent with the details of the strain–time curves. The sensitivity gauge under different strain waveforms was 5.9, which was close to the results of the tensile tests, indicating repeatability and reliable sensing performance of the core-sheath fiber sensor (Fig. 5f). The electrical response under 10000 cycles remained steady within an acceptable range, demonstrating excellent electromechanical durability (Fig. S8).

The core-sheath fiber exhibited a rate-dependent mechanical property; thus, the strain rate dependency of the electromechanical properties gained our interest. Cyclic tensile tests were carried out on the fiber sensors. The strain was set at 0.1, and the frequency increased from

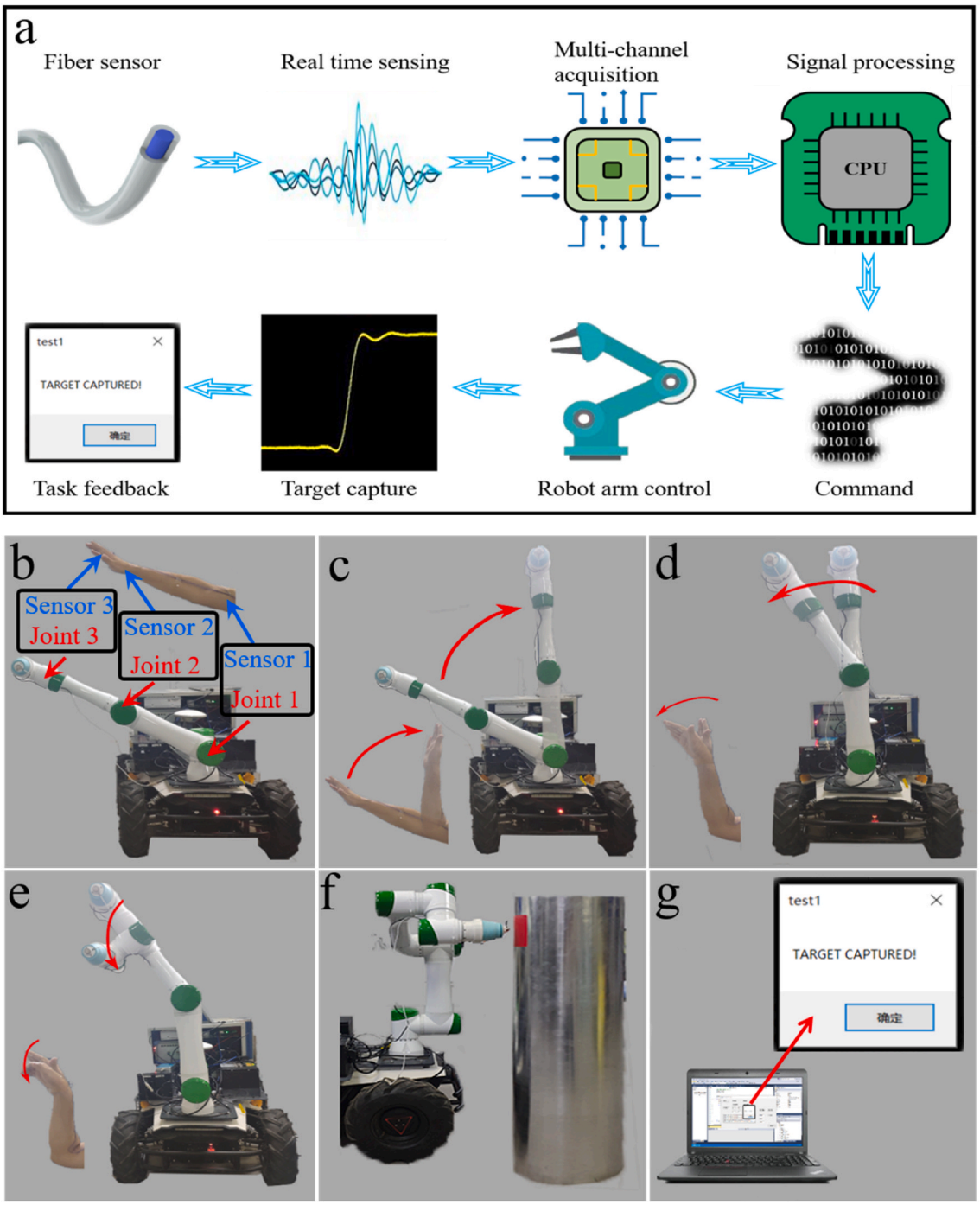

Fig. 7. Application of core-sheath fiber sensors in human–robot interaction. Schematic of human–robot interaction (a). The fiber sensors attached on human and robot arms (b). The fiber sensors attached on the elbow, wrist, and index finger were used to control three corresponding rotatable joints separately. The gesture recognition of elbow (c), wrist (d), and index finger (e) and the movement control of the corresponding robot arm joint. The detector at the end of the robot arm capturing the target after three-step gesture control (f) and the feedback to the control terminal (g).

0.005 to 1 Hz (Fig. 5g). The corresponding $\dot{\varepsilon}$ increased from 0.01 to 0.2. Interestingly, $\Delta R/R_0$ increased with the applied $\dot{\varepsilon}$. In addition, the electrical response under cyclic tensile tests at high frequencies exhibited a shoulder peak pattern (Fig. S9), which was also observed in other sensors based on a viscoelastic matrix [46]. To avoid the complicated shoulder peak pattern, a trapezoidal waveform strain was applied instead (Fig. 5h). First, the fiber was stretched at different strain rates by 100%, which was the limit of the linear correlation region. The strain was maintained for approximately 250 s before release. The sensitivity gauge (G) showed a strong dependency on the strain rate $\dot{\varepsilon}$ (Fig. 5i).

$$G \propto (\dot{\varepsilon})^{-\alpha} \tag{6}$$

where α is the exponent. The data agreed well with the theory, giving $\alpha = -0.14$ (Eqs. S1–S10).

The core-sheath fiber sensor also exhibited an outstanding sensing performance for compression and bending deformations. A fiber with a length of 20 mm was placed on a flat surface, and an indenter with a radius of 8 mm was applied to compress the fiber (Fig. 6a). $\Delta R/R_0$ increased from 0 to 0.023 as the fiber was compressed by 0.2 mm and was then recovered as the compression was removed. In addition, the

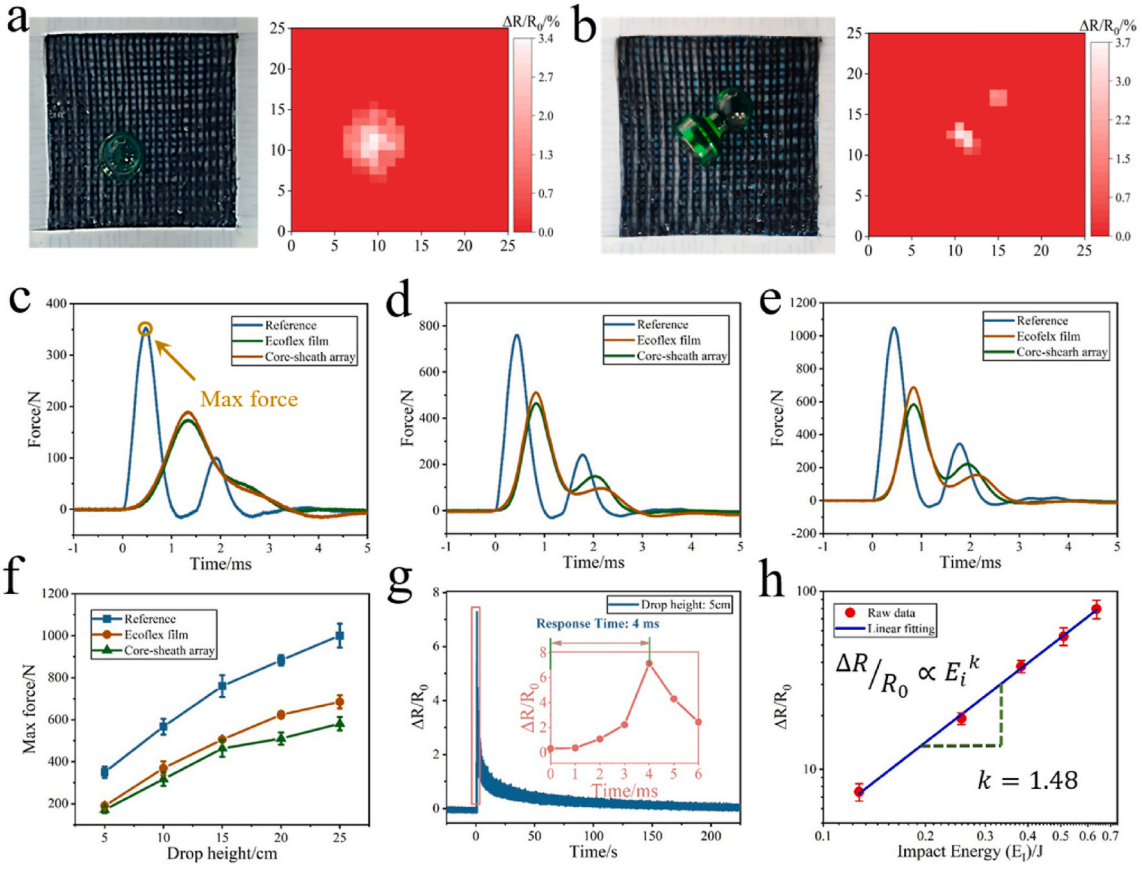

Fig. 8. Application of the printed arrays. A double-layered array (45 mm × 45 mm × 3.0 mm) was used to monitor the pressure and position of standing chess (a) and lying chess (b). Plot of force vs. time from the impact tests with drop heights of 5 cm (c), 15 cm, (d) and 25 cm (e). Plot of maximum force vs. drop height (f). Resistance response as the impact hammer impacted on the array from a drop height of 5 cm (g). The $\Delta R/R_0$ dependency upon impact energy, E_I (h).

values of $\Delta R/R_0$ changed reproducibly and regularly. The fiber sensor exhibited a linear resistance dependency on compression deformation with a sensitivity of 0.042 mm^{-1} (Fig. 6b). As the compressed length was relatively shorter than the fiber length, the compression sensitivity was relatively lower. However, a fiber sensor that can capture a compression force as low as 3 mN is still remarkable. The fiber sensor could also detect bending deformations. A fiber with a length of 60 mm was attached to a plastic cantilever beam (Fig. 6d, inset). One side of the beam was fixed by a clamp, and the other side was bent to a designed angle, which was captured by a camera. In addition, the electrical responses were recorded (Fig. 6c). $\Delta R/R_0$ increased from 0 to 0.027 as the plastic plate was bent from 0° to 30° and further increased to 0.11 as the bending angle was increased to 120°. Moreover, the fiber exhibited good electromechanical stability for at least 10 cycles. The sensitivity gauge value in the 30°–120° region was 0.9×10^{-3} and increased to 3.6×10^{-3} in the 120°–180° region (Fig. 6d). In summary, the fiber sensor with high flexibility exhibited excellent electromechanical properties under tension, compression, and bending, showing great potential in wearable electronics and human–robot interaction.

3.3. Applications of core-sheath fibers and patterns

Fig. 7a depicts the process of human–robot interaction, which mainly includes the capture of human gesture, robot arm control, and feedback. Owing to their outstanding sensing performance, three fiber sensors were attached to the elbow, wrist, and index finger. They were used to capture human gestures to control the movement of the corresponding joints (Fig. 7b). The captured signals were transferred to the control terminal using a multichannel signal acquisition system for signal processing and analysis. The corresponding commands were then delivered to control the movement of the robot arm. For example, as the forearm was bent vertically, the generated electrical signals were collected by sensor 1 and further analyzed in the control terminal. Then, the corresponding rotation commands were sent to Joint 1, to rapidly lift the robot arm vertically (Fig. 7c and Movie. S). Similarly, the bending of the wrist and index finger controlled the rotation of Joint 2 (Fig. 7d) and Joint 3 (Fig. 7e), respectively. After the three-step control, the detector at the end of the robot arm successfully captured the target, as shown by the red tape (Fig. 7f). Then, the feedback message was presented to workers for the subsequent operations. In summary, the human–robot interactions were effectively accomplished using the core-sheath fiber sensors, which could be further used in medical treatment, dangerous object detection, and fire rescue.

Subsequently, 25 horizontal fibers were printed on 25 vertical fibers to construct a core-sheath fiber array as an artificial skin to simultaneously detect the pressure and position of an external stimulus. The reconstructed maps clearly and effectively show the pressure distribution induced by a lying and standing chess (1.5 g) (Fig. 8a and b). Moreover, owing to the typical shear-stiffening property of SSG, the core-sheath array had a safeguarding function, which could protect people from external harm. The safeguarding performance was illustrated through drop tower tests. A drop hammer (0.24 kg) was dropped from a certain height and impacted on the core-sheath array, and a force sensor under the array recorded the penetrated force. For comparison, an Ecoflex film with the same thickness was also investigated. Apparently, without a protective layer, the penetrated force signal (referred to as reference) increased sharply to a maximum value (352 N) as the drop hammer from a height of 5 cm impacted on the force sensor. Then, the penetrated force decreased quickly to zero in 1 ms (Fig. 8c). Compared with the other specimens, the core-sheath array exhibited the smallest

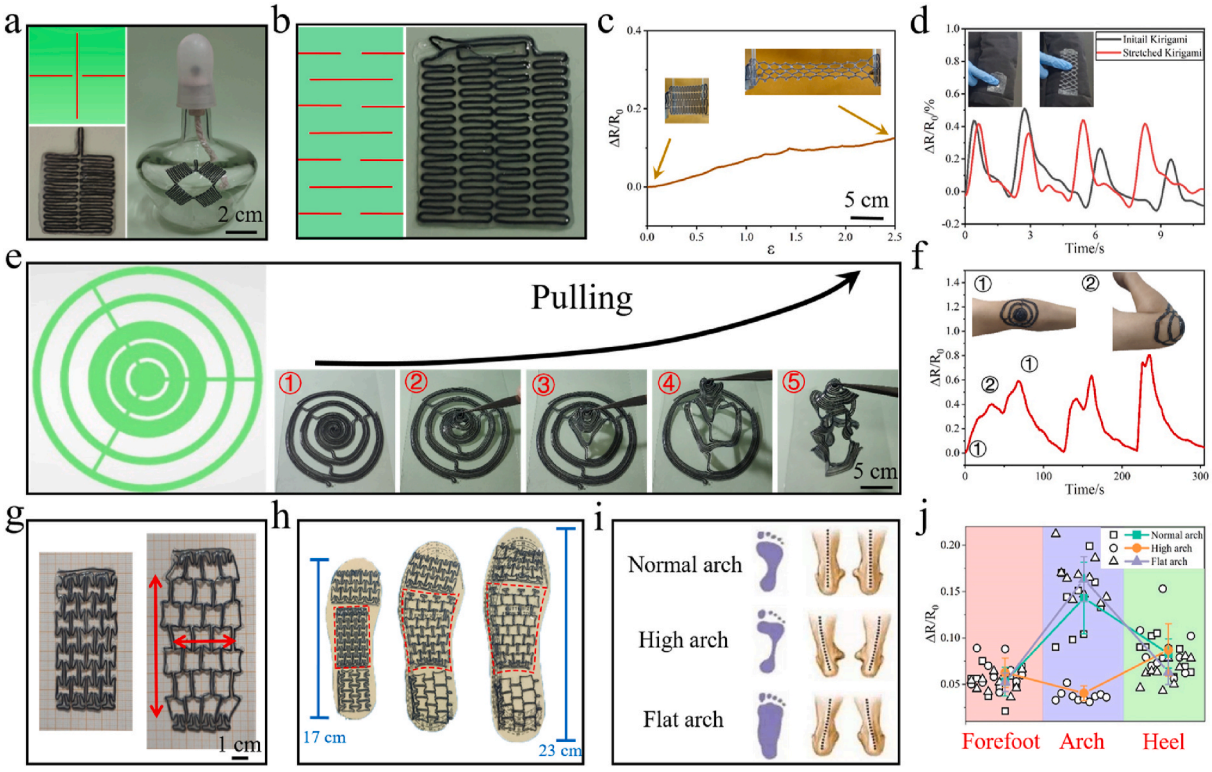

Fig. 9. Kirigami-inspired patterns for complex and irregular surfaces. Fractal cut kirigami pattern (a). Parallel kirigami pattern (b) and its resistance variations under tensile loadings (c). Resistance response of parallel kirigami pattern to finger press at the initial and stretched states (d). A schematic of the circular kirigami-patterned planar core-sheath film, which was pulled into a 3D structure (e). Resistance signals recorded by the circular kirigami pattern, which was attached on the bending elbow (f). Photos showing the negative Poisson's ratio property of the core-sheath film (g). Core-sheath films, which were adaptive to shoe pads with different sizes (h). Schematics of normal, high, and flat arcs (i). Monitoring of gaits (j).

peak force of 174 N, which was 51% lower than that of the reference group, indicating its excellent force dissipation property.

When the hammer stroked on the SSG-CNT composites, a shear-stiffening effect occurred, and the dramatic increase in the rate-dependent rigidity endured and dampened the impact force effectively. As the drop height increased from 5 to 15 and 25 cm (Fig. 8d and e), the maximum force also increased. Owing to the protection of the core-sheath array, the penetration force decreased (Fig. 8f). The core-sheath array not only dissipated the impact force but also captured the stimuli of the impact by recording its electrical response (Fig. 8g). Evidently, the resistance increased abruptly to a peak value in 4 ms after the impact, indicating excellent dynamic sensing and fast response capability. The electrical response showed a strong dependency on the impact energy, $E_I = mgh$, where m is the mass of the drop hammer, g is the gravity constant, and h is the drop height. Reasonably, with the increase in E_I, the deformation of the core-sheath array also increased and finally induced a larger resistance change. According to Ref. [36], $\Delta R/R_0$ is related to E_I as follows:

$$\frac{\Delta R}{R_0} \propto {E_I}^k \tag{7}$$

where k is the correlation coefficient. The data agreed well with the theory, yielding $k = 1.48$. In summary, the core-sheath array exhibited excellent static and dynamic sensing properties and safeguarding performance, indicating great potential for multifunctional wearable electronics.

Most skin-mounted wearable electronics require conformal contact with irregular biological surfaces [24]. Thus, the kirigami-inspired scheme was developed to extend planar electronics into a 3D adjustable form through rational cut designs. Fig. 9a showed an example with a fractal pattern, which transformed the printed planar core-sheath film into an out-of-plane shape-adjustable structure. The red lines represent cut lines. The small amount of material between adjacent cuts served as hinges between the square units, providing a high degree of expandability. Thus, the fractal pattern conformed to the irregular convex geometry of the lamp through the rotation of the square units. Additionally, no damage was observed during the shape transformation process, indicating the stability of the 3D-adjustable pattern. This feasible kirigami-inspired route also made the 2D film adaptable and portable (Fig. 9b). As the parallel kirigami pattern was stretched, the parallel arrangement of the slits caused the fibers to bend upon tensile loading, thereby reducing tensile deformations (Fig. 9c). Thus, $\Delta R/R_0$ was only approximately 0.13 at $\varepsilon = 2.5$, which was relatively smaller than the results for the core-sheath fiber. The relatively small change in conductivity made the parallel kirigami pattern adaptive to size-varied surfaces still with high sensitivity (Fig. 9d). Fig. 9e shows a circular kirigami pattern that could be pulled into an out-of-plane shape--adjustable cone structure. Compared with the normal circular film (Fig. S10), the circular kirigami pattern could effectively enhance adhesion to the varying and curved surfaces of the bending elbow (Fig. 9f). Moreover, the arm movement could be captured by the resistance response simultaneously, which was substantially important for application of next-generation wearable electronics in complex clinical and biological conditions.

Furthermore, to introduce portability and customize the macroscopic physical properties, the topological parameters and structural arrangement of the fibers were designed to fabricate auxetic mechanical metamaterials (negative Poisson's ratio metamaterial). Metamaterial films (Fig. 9g), which expand transversally when axially stretched, are widely used in flexible electronics, and contribute to the development of advanced functional materials [47,48]. Its unique negative Poisson's ratio property makes the metamaterial films adaptive to shoe pads of

different sizes (Fig. 9h). As the shoe pad length increased from 17 to 23 cm (size 24 to 36, Chinese standard), the metamaterial films could still cover the surfaces (forefoot, arch, and heel), which were further used to monitor abnormal gait. As shown in Fig. 9i, the arch, which is used for balance and buffer, is an important parameter for gait. A person with a flat arch may bend his legs inward and hit them against each other while walking, which may cause falling. A high arch could make the person's toes point toward each other and scrape against the ground, leading to overly worn joints. Thus, gaits were monitored to improve human health (Fig. 9j). The $\Delta R/R_0$ values of flat and high arches were substantially different from those of a normal arch, thereby helping in making early diagnosis and providing essential evidence for medical advice and treatment. Moreover, the application of portable metamaterial films provides a feasible way to monitor people's gait regardless of their feet sizes, indicating excellent adaptability. In summary, the potential application of SSG-based wearable electronics in complex and variable conditions were substantially expanded owing to the scalability and adaptability of the 3D printing technique and kirigami-inspired patterns.

4. Conclusion

In summary, deployable core-sheath wearable electronics were developed using a coaxial 3D printing technique and kirigami-inspired patterns. The core-sheath fiber sensor, which was successfully applied in human–robot interaction, exhibited high sensitivity to various stimuli with a high accuracy of ~3 mN and high mechanical durability (>10000). Owing to its rate-dependent electromechanical properties, the core-sheath array could buffer 51% of the impact force and detect dynamic stimuli with a short response time of 4 ms. Additionally, the incorporation of kirigami patterns provides an effective strategy to expand the 2D planar electronics into mechanically adjustable 3D structures that can be conformably attached to curved/size-varied irregular biological surfaces. More complex 3D electronic systems that utilize both the fabrication customization superiority of the 3D printing system as well as the compliant and adjustable mechanism offered by the kirigami-induced deformability have great potential for emerging wearable electronics applications in clinical and biological conditions that are complex and dynamic.

Author statement

Shuaishuai Zhang: performed all the experiments and wrote the draft of the manuscript. Shouhu Xuan, Sheng Wang and Xinglong Gong revised and discussed the manuscript. Shuaishuai Zhang, Yuxiang Zheng, Run Yang and Erbao Dong carried out human-robot interaction experiments. Liang Lu provided advices for waking gait monitoring tests and related data analysis.

Declaration of competing interest

The authors declare that they have no known competing financial interests or personal relationships that could have appeared to influence the work reported in this paper.

Acknowledgements

Financial support from the National Natural Science Foundation of China (Grant No. 11822209, 11802303, 11772320, 11972032), the Fundamental Research Funds for the Central Universities (WK2480000007), the Strategic Priority Research Program of the Chinese Academy of Sciences (Grant No. XDB22040502), and the Joint Fund of USTC-National Synchrotron Radiation Laboratory (KY2090000055) are gratefully acknowledged.

Appendix A. Supplementary data

Supplementary data to this article can be found online at https://doi.org/10.1016/j.compscitech.2021.109041.

References

[1] H. Lukas, C. Xu, Y. Yu, W. Gao, Emerging telemedicine tools for remote COVID-19 diagnosis, monitoring, and management, ACS Nano 14 (12) (2020) 16180–16193.
[2] Y.J. Ma, Y.C. Zhang, S.S. Cai, Z.Y. Han, X. Liu, F.L. Wang, et al., Flexible hybrid electronics for digital healthcare, Adv. Mater. 32 (15) (2020) 23.
[3] Y. Yu, J. Nassar, C.H. Xu, J.H. Min, Y.R. Yang, A. Dai, et al., Biofuel-powered soft electronic skin with multiplexed and wireless sensing for human-machine interfaces, Sci Robot 5 (41) (2020) 13.
[4] S. Jung, J.H. Kim, J. Kim, S. Choi, J. Lee, I. Park, et al., Reverse-micelle-induced porous pressure-sensitive rubber for wearable human-machine interfaces, Adv. Mater. 26 (28) (2014) 4825–4830.
[5] X.L. Zhao, S. Yang, Z.J. Sun, N. Cui, P.F. Zhao, Q.X. Tang, et al., Enhancing the intrinsic stretchability of micropatterned gold film by covalent linkage of carbon nanotubes for wearable electronics, ACS Appl Electron Mater 1 (7) (2019) 1295–1303.
[6] W. Liu, Y.H. Huang, Y.D. Peng, M. Walczak, D. Wang, Q. Chen, et al., Stable wearable strain sensors on textiles by direct laser writing of graphene, ACS Appl Nano Mater 3 (1) (2020) 283–293.
[7] P. Li, Y.K. Zhang, Z.J. Zheng, Polymer-assisted metal deposition (PAMD) for flexible and wearable electronics: principle, materials, printing, and devices, Adv. Mater. 31 (37) (2019) 16.
[8] X.-Y. Yin, Y. Zhang, X. Cai, Q. Guo, J. Yang, Z.L. Wang, 3D printing of ionic conductors for high-sensitivity wearable sensors, Mater Horiz 6 (4) (2019) 767–780.
[9] Z. Wang, W. Gao, Q. Zhang, K. Zheng, J. Xu, W. Xu, et al., 3D-printed graphene/polydimethylsiloxane composites for stretchable and strain-insensitive temperature sensors, ACS Appl. Mater. Interfaces 11 (1) (2019) 1344–1352.
[10] Z. Wang, X. Guan, H. Huang, H. Wang, W. Lin, Z. Peng, Full 3D printing of stretchable piezoresistive sensor with hierarchical porosity and multimodulus architecture, Adv. Funct. Mater. 29 (11) (2019) 1807569.
[11] S.Z. Guo, K. Qiu, F. Meng, S.H. Park, M.C. McAlpine, 3D printed stretchable tactile sensors, Adv. Mater. 29 (27) (2017) 1701218.
[12] T. Xiao, C. Qian, R. Yin, K. Wang, Y. Gao, F. Xuan, 3D printing of flexible strain sensor array based on UV-curable multiwalled carbon nanotube/elastomer composite, Adv Mater Technol 6 (1) (2021) 2000745.
[13] Y. Gao, M. Xu, G. Yu, J. Tan, F. Xuan, Extrusion printing of carbon nanotube-coated elastomer fiber with microstructures for flexible pressure sensors, Sens. Actuators, A A. 299 (2019) 111625.
[14] Y. Gao, G. Yu, T. Shu, Y. Chen, W. Yang, Y. Liu, et al., 3D-printed coaxial fibers for integrated wearable sensor skin, Adv Mater Technol 4 (10) (2019) 1900504.
[15] Y. Zhang, W. Zhang, G. Ye, Q. Tan, Y. Zhao, J. Qiu, et al., Core-sheath stretchable conductive fibers for safe underwater wearable electronics, Adv Mater Technol 5 (1) (2020) 1900880.
[16] T. Hu, S. Xuan, L. Ding, X. Gong, Liquid metal circuit based magnetoresistive strain sensor with discriminating magnetic and mechanical sensitivity, Sens. Actuators, B 314 (2020) 128095.
[17] M.A.H. Khondoker, D. Sameoto, Fabrication methods and applications of microstructured gallium based liquid metal alloys, Smart Mater. Struct. 25 (9) (2016), 093001.
[18] M.A.H. Khondoker, A. Ostashek, D. Sameoto, Direct 3D printing of stretchable circuits via liquid metal co-extrusion within thermoplastic filaments, Adv. Eng. Mater. 21 (7) (2019) 1900060.
[19] Z. Tang, S. Jia, X. Shi, B. Li, C. Zhou, Coaxial printing of silicone elastomer composite fibers for stretchable and wearable piezoresistive sensors, Polymers 11 (4) (2019) 666.
[20] S. Xu, Y. Zhang, L. Jia, K.E. Mathewson, K.-I. Jang, J. Kim, et al., Soft microfluidic assemblies of sensors, circuits, and radios for the skin, Science 344 (6179) (2014) 70–74.
[21] J. Kim, E.-F. Chou, J. Le, S. Wong, M. Chu, M. Khine, Soft wearable pressure sensors for beat-to-beat blood pressure monitoring, Adv Healthcare Mater 8 (13) (2019) 1900109.
[22] J. Choi, R. Ghaffari, L.B. Baker, J.A. Rogers, Skin-interfaced systems for sweat collection and analytics, Sci Adv 4 (2) (2018) 3921.
[23] S.J.P. Callens, A.A. Zadpoor, From flat sheets to curved geometries: origami and kirigami approaches, Mater. Today 21 (3) (2018) 241–264.
[24] R. Zhao, S. Lin, H. Yuk, X. Zhao, Kirigami enhances film adhesion, Soft Matter 14 (13) (2018) 2515–2525.
[25] T.C. Shyu, P.F. Damasceno, P.M. Dodd, A. Lamoureux, L. Xu, M. Shlian, et al., A kirigami approach to engineering elasticity in nanocomposites through patterned defects, Nat. Mater. 14 (8) (2015) 785–789.
[26] S. Charkhabi, Y.J. Chan, D.-G. Hwang, S.T. Frey, M.D. Bartlett, N.F. Reuel, Kirigami-enabled, passive resonant sensors for wireless deformation monitoring, Adv Mater Technol 4 (5) (2019) 1800683.
[27] E.E. Evke, D. Meli, M. Shtein, Developable rotationally symmetric kirigami-based structures as sensor platforms, Adv Mater Technol 4 (12) (2019) 1900563.
[28] Z. Zhang, Y. Yu, Y. Tang, Ys Guan, Y. Hu, J. Yin, et al., Kirigami-inspired stretchable conjugated electronics, Adv Electron Mater 6 (1) (2019) 1900929.

[29] C. Yang, H. Zhang, Y. Liu, Z. Yu, X. Wei, Y. Hu, Kirigami-inspired deformable 3D structures conformable to curved biological surface, Adv. Sci. 5 (12) (2018) 1801070.
[30] M.A. Abtew, F. Boussu, P. Bruniaux, C. Loghin, I. Cristian, Ballistic impact mechanisms: a review on textiles and fibre-reinforced composites impact responses, Compos. Struct. 223 (2019) 41.
[31] J. Chen, H. Xie, X. Lai, H. Li, J. Gao, X. Zeng, An ultrasensitive fire-warning chitosan/montmorillonite/carbon nanotube composite aerogel with high fire-resistance, Chem. Eng. J. 399 (2020) 125729.
[32] Y. Huang, L.-Q. Tao, J. Yu, Z. Wang, C. Zhu, X. Chen, Integrated sensing and warning multifunctional devices based on the combined mechanical and thermal effect of porous graphene, ACS Appl. Mater. Interfaces 12 (47) (2020) 53049–53057.
[33] S. Wang, L. Ding, Y. Wang, X. Gong, Multifunctional triboelectric nanogenerator towards impact energy harvesting and safeguards, Nanomater. Energy 59 (2019) 434–442.
[34] Y. Wang, X. Gong, S. Xuan, Study of low-velocity impact response of sandwich panels with shear-thickening gel cores, Smart Mater. Struct. 27 (6) (2018), 065008.
[35] F. Yuan, S. Liu, J. Zhou, X. Fan, S. Wang, X. Gong, A smart Kevlar-based triboelectric nanogenerator with enhanced anti-impact and self-powered sensing properties, Smart Mater. Struct. 29 (12) (2020) 125007.
[36] C.S. Boland, U. Khan, G. Ryan, S. Barwich, R. Charifou, A. Harvey, et al., Sensitive electromechanical sensors using viscoelastic graphene-polymer nanocomposites, Science 354 (6317) (2016) 1257–1260.
[37] J. Zhou, S. Wang, F. Yuan, J. Zhang, S. Liu, C. Zhao, et al., Functional Kevlar-based triboelectric nanogenerator with impact energy-harvesting property for power source and personal safeguard, ACS Appl. Mater. Interfaces 13 (5) (2021) 6575–6584.
[38] Y. Wang, S. Wang, C. Xu, S. Xuan, W. Jiang, X. Gong, Dynamic behavior of magnetically responsive shear-stiffening gel under high strain rate, Compos. Sci. Technol. 127 (2016) 169–176.
[39] W.H. Shih, W.Y. Shih, S.I. Kim, J. Liu, I.A. Aksay, Scaling behavior of the elastic properties of colloidal gels, Phys. Rev. 42 (8) (1990) 4772–4779.
[40] A.R. Payne, The dynamic properties of carbon black-loaded natural rubber vulcanizates. Part I, J. Appl. Polym. Sci. 6 (1962) 57–63.
[41] X.W. Zhang, Y. Pan, Q. Zheng, X.S. Yi, Time dependence of piezoresistance for the conductor-filled polymer composites, J. Polym. Sci., Part B: Polym. Phys. 38 (21) (2000) 2739–2749.
[42] D. Stauffer, Scaling theory of percolation clusters, Phys. Rep. 54 (1) (1979) 1–74.
[43] I. Balberg, D. Azulay, D. Toker, O. Millo, Percolation and tunneling in composite materials, Int. J. Mod. Phys. B 18 (15) (2004) 2091–2121.
[44] M. Sanchez, R. Moriche, X.F. Sanchez-Romate, S.G. Prolongo, J. Rams, A. Urena, Effect of graphene nanoplatelets thickness on strain sensitivity of nanocomposites: a deeper theoretical to experimental analysis, Compos. Sci. Technol. 181 (2019) 107697.
[45] B.N. Turner, R. Strong, S.A. Gold, A review of melt extrusion additive manufacturing processes: I. Process design and modeling, Rapid Prototyp. J. 20 (3) (2014) 192–204.
[46] H. Yang, X. Yao, L. Yuan, L. Gong, Y. Liu, Strain-sensitive electrical conductivity of carbon nanotube-graphene-filled rubber composites under cyclic loading, Nanoscale 11 (2) (2019) 578–586.
[47] A. Ebrahimi, W. Withayachumnankul, S. Al-Sarawi, D. Abbott, High-sensitivity metamaterial-inspired sensor for microfluidic dielectric characterization, IEEE Sensor. J. 14 (5) (2014) 1345–1351.
[48] W. Withayachumnankul, K. Jaruwongrungsee, A. Tuantranont, C. Fumeaux, D. Abbott, Metamaterial-based microfluidic sensor for dielectric characterization, Sens. Actuators, A A. 189 (2013) 233–237.